



3D microextrusion of eco-friendly water based cer-cer composite pastes for hydrogen separation

Andrea Bartoletti^{a,b,*}, Alex Sangiorgi^{a,**}, Elisa Mercadelli^a, Cesare Melandri^a, Angela Gondolini^a, Sandra García-González^{c,d}, Laia Ortiz-Membrado^{c,d}, Miguel Morales^{c,d}, Emilio Jimenez-Pique^{c,d}, Alessandra Sanson^a

^a Institute of Science, Technology and Sustainability for Ceramics (ISSMC) of the National Research Council (CNR), Via Granarolo 64, I-48018, Faenza, RA, Italy

^b Department of Chemical Sciences, Università degli Studi di Padova, Via Marzolo 1, 35131, Padova, Italy

^c CIEFMA—Department of Materials Science and Engineering, EEBE—Campus Diagonal Besòs, Universitat Politècnica de Catalunya—BarcelonaTech, 08019, Barcelona, Spain

^d Barcelona Research Center in Multiscale Science and Engineering, EEBE—Campus Diagonal Besòs, Universitat Politècnica de Catalunya—BarcelonaTech, 08019, Barcelona, Spain

ARTICLE INFO

Handling Editor: Dr P Colombo

Keywords:

BCZY-GDC composite

Water-based inks

Membranes

Hydrogen

Osmotic drying

High-speed nanoindentation

ABSTRACT

Ceramic membranes operating at high-temperatures are a key-technology for hydrogen separation processes. Cer-cer composites based on $\text{BaCe}_{0.65}\text{Zr}_{0.20}\text{Y}_{0.15}\text{O}_{3-\delta}\text{-Gd}_{0.2}\text{Ce}_{0.8}\text{O}_{2-\delta}$ have gained increasing attention as asymmetric membranes for H_2 purification, for their high proton-electron conductivity, 100% selectivity, temperature and chemical stability, and intrinsic lower costs compared with the Pd-based technologies. Here, BCZY-GDC composite parts were successfully fabricated for the first time by microextrusion. Water-based pastes with different solid loadings and suitable rheological properties were formulated and printed in single or multilayer structures without nozzle clogging. After deposition, the samples were osmotically dried in concentrated PEG solutions in order to obtain cracks-free green bodies. The further process optimization allowed the production of planar BCZY-GDC ceramics to be potentially applied in asymmetric membrane structures. The mechanical properties of the as-obtained single and multilayer structures as well as of the interface between filaments were assessed through different nanoindentation techniques.

1. Introduction

The energy crisis and environmental pollution have been dramatically aggravated by global socio-economic activities. In this context, hydrogen is expected to play a key-role within the world's energy transition that has been ongoing over the past decade [1]. Starting from 2019, the development of an Hydrogen Economy is in fact a priority for the European Community, and with the European Green Deal, the net reduction of greenhouse gas emissions is expected by 2050 [2]. Nowadays, most of the hydrogen produced worldwide (around 96 %) comes from fossil fuels by steam reforming or partial oxidation of methane, coal gasification and natural gas pyrolysis (the so called “blue” or “grey” hydrogen) [1–3]. However, hydrogen produced using these technologies has significant amounts of impurities (such as CO , CO_2 , H_2O) and needs additional purification [4–6].

In this framework, proton conducting ceramic membranes represent a cost-effective and robust solution for its purification at the high temperatures used in the hydrogen production reactors ($>500^\circ\text{C}$), unlocking the possibility of processes intensification. Moreover, there is an increasing interest in the use of ceramic membranes as ion conducting catalytic membrane reactor, to combine separation and catalytic reaction processes [7]. All-ceramic mixed proton–electron conductor membranes, such as doped perovskites based on the barium cerate-zirconate solid solutions are the most promising alternatives to obtain low-cost H_2 purification devices.

Among these materials, dense ceramic-ceramic composites of $\text{BaCe}_{0.65}\text{Zr}_{0.20}\text{Y}_{0.15}\text{O}_{3-\delta}$ and $\text{Ce}_{0.8}\text{Gd}_{0.2}\text{O}_{2-\delta}$ (BCZY-GDC) represent a suitable compromise between good stability in CO_2 [8] and H_2S reach atmosphere [9], high ambipolar conductivity and mechanical stability [10–12]. Since the hydrogen permeation is generally inversely

* Corresponding author. Via Granarolo, 64, 48018, Faenza, RA, Italy.

** Corresponding author. Via Granarolo, 64, 48018, Faenza, RA, Italy.

E-mail addresses: andrea.bartoletti@issmc.cnr.it (A. Bartoletti), alex.sangiorgi@issmc.cnr.it (A. Sangiorgi).

proportional to the thickness of the membrane, performances may be enhanced with an asymmetric architecture formed by a thin dense layer supported by a thick porous substrate [13]. The thinnest is the active layer, the lower would be its bulk diffusion resistance [14].

Another aspect to consider is the support microstructure, generally consisting of randomly oriented pores obtained through the pyrolysis of specific pore formers [13,15]. To enhance the membrane performances, one strategy is to design porous oriented architectures capable of conveying large quantities of gas without decreasing the mechanical resistance of the membrane. In addition, the obtainment of well oriented pores can facilitate the catalyst impregnation. To reach this goal one way is to exploit the peculiar advantages of innovative shaping techniques for this field, such as ice templating or Additive Manufacturing (AM).

Recently, promising results have been published regarding the use of freeze casting for the fabrication of ceramic supports for gas separation devices with a high degree of unidirectional porosity [16–19].

Additive manufacturing offers several advantages compared to conventional techniques, as it is a tool-free process (therefore can reduce both wear and machine setup times), and also provides more flexibility in product design and customised solutions. Moreover, from an economical point of view AM is considered less expensive for the production of small production volumes and/or for complex ceramics parts respect to traditional shaping techniques [20]. However, the commercialisation of such processes and products has regarded mainly metallic items, while ceramics are still facing considerable issues that have left their processing by additive manufacturing at a preliminary stage [21].

Among the AM techniques, DIW is considered the cheapest, the most versatile and easiest scalable technique to fabricate complex parts with high speed of production [20,22,23]. Recently, M. Cannio et al., [24], reported the production of alcoholic-based $\text{BaCe}_{0.65}\text{Zr}_{0.20}\text{Y}_{0.15}\text{O}_{3-\delta}$ - $\text{Gd}_{0.15}\text{Ce}_{0.85}\text{O}_{2-\delta}$ slurries with suitable stability and rheological behaviour for Direct Ink Writing (DIW). However, this study shows only preliminary results without providing any information about both the as-printed and sintered structures potentially obtainable by DIW.

Here, BCZY-GDC composite ceramics specimens were successfully printed and consolidated for the first time through Direct Ink Writing (DIW). Different eco-friendly water-based pastes with increasing amounts of solid loading were successfully obtained through the careful optimization of each step concerning the components mixing methodology. All the processing parameters were thoroughly investigated in order to produce planar and defect-free BCZY-GDC structures with comparable mechanical properties to samples obtained through traditional shaping techniques (i.e. die pressing, tape casting).

Finally, several nanoindentation tests were carried out to determine the quality of BCZY-GDC parts fabricated by DIW. Newer instrumented indentation techniques allow automated measurement of elastic modulus and hardness at different scales, down to the sub-micron range, without needing direct measurements of the residual hardness impressions. Recently, the development of high-speed nanoindentation techniques has enabled the acquisition of large spatial datasets that can generate mechanical maps of the investigated material. Such data, statistically treated, can also be deconvoluted to assess the intrinsic mechanical properties of the constitutive phases or constituents [25–32]. In this work, E and H values of each individual constituent of the composite were estimated from mechanical property maps and the data distribution of large arrays by deconvolution using, for the first time, the 1D Gaussian fitting method. Moreover, the elastic modulus (*E*) and hardness (*H*) on the single-layer structure as well as at the interface between filaments in multi-layered samples were also assessed through “conventional” nanoindentation analysis.

Table 1

Ink compositions expressed in wt. %.

	BCZY-GDC (1:1)	Ethylene Glycol	Glycerol	Pluronic solution (25 wt %)
INK_A	83	6	5	6
INK_B	80	6	5	9
INK_C	77	6	5	12



Fig. 1. Picture of Ink_B after mixing at the planetary mixer.

2. Materials and methods

2.1. Materials

$\text{BaCe}_{0.65}\text{Zr}_{0.20}\text{Y}_{0.15}\text{O}_{3-\delta}$ (BCZY, s.s.a. = 4,92 m²/g and d_{50} = 1,1 μm, Marion Technologies, France) and $\text{Ce}_{0.8}\text{Gd}_{0.2}\text{O}_{2-\delta}$ (GDC, s.s.a. = 5,60 m²/g and d_{50} = 0,21 μm Fuel Cell Materials, USA) were selected as the starting ceramic powders. Ethylene Glycol (99,99 %, Sigma Aldrich, UK) was chosen as humectant to slow down water evaporation, Glycerol (87,00 %, Merck, Germany) and Pluronic F-127 (Sigma Aldrich, UK) where used respectively as plasticiser and binder. Polyethylene glycol 200 (PEG200, Merck, Germany), Polyethylene glycol 400 (PEG 400, Sigma Aldrich, UK), Polyethylene glycol 600 (PEG600, Fluka, Germany) and Polyethylene glycol 2000 (PEG2000, Merck, Germany) were used as liquid desiccants.

2.2. Ink preparation

A Pluronic stock solution was prepared by stirring Pluronic F-127 powder into a flask of Milli-Q water at 0–4 °C until a 25 wt % solution is obtained. The solution was left in a refrigerator at 4 °C for 24 h, allowing bubbles to dissipate [33]. Water-based ceramic pastes were obtained following a previously optimized methodology [34]. First, stoichiometric amounts of BCZY and GDC (1:1 vol) were treated in a high-energy planetary mill (Fritsch, Pulverisette 6) using zirconia beads and jar with absolute ethanol as solvent, followed by a 15 min sonicating treatment (Sonicator, ultrasonic processor XL, USA). Then Ethylene Glycol and Glycerol were added to the suspension and EtOH was evaporated under mechanical stirring at room temperature. The resulting wet paste was then grounded into a mortar with a pestle for 15 min to break down any agglomerates. Finally, Inks were prepared by mixing small aliquots of the wet grounded paste with the binder solution in a continuous planetary mixer (Thinky ARE-500CE, Thinky Corporation, Japan). Before printing, a prolonged defoaming cycle of 10' at 400 rpm were performed to eliminate trapped bubbles. Three inks with different amounts of binder solution (i.e. Pluronic F-127 and water) were successfully obtained and their theoretical compositions are given in Table 1. The visual representation of Ink_B is shown in Fig. 1 as a reference, since no macroscopic differences were observed between the produced pastes."

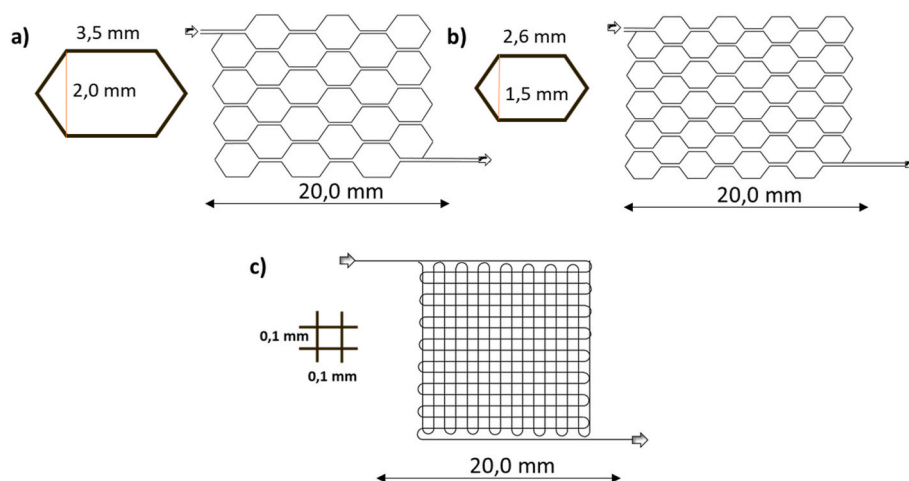


Fig. 2. Different paths used in this study: Large (a) and small (b) hexagonal mesh geometries; grid-type (c) shapes.

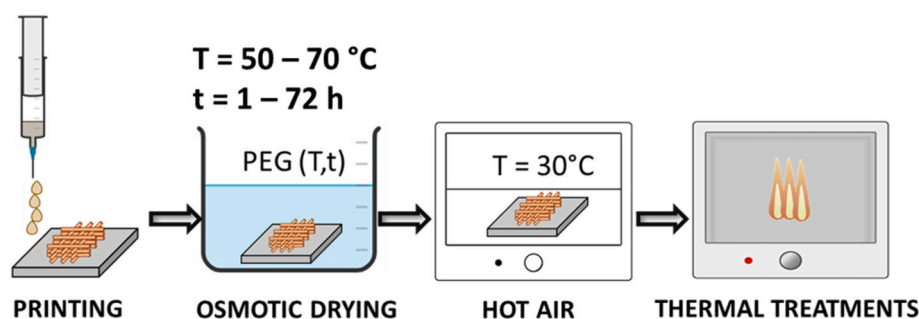


Fig. 3. Schematic representation of the post printing operations.

2.3. Support fabrication

The depositions were carried out with a stand-alone multiple heads machine (XCEL, AUREL, Italy) equipped with a micro extruder (ECO-PEN 450, ViscoTec, Germany) using conical needles with 0.41 mm nozzle size. The paste extrusion flow rate was set at 0.1 ml/min, while the distance h between the extruder nozzle and substrate, the stage moving speed (v) and the line spacing between the adjacent filaments (w) were carefully optimized to obtain high resolution structures with different designs. Samples were printed on dense Al_2O_3 supports using honeycomb designs with different mesh sizes in order to obtain structures with different porosity levels (45% and 30% of open porosity) and suitable mechanical properties; simple grid-type geometries were also considered. The 2D representations of the selected designs are shown in Fig. 2.

2.4. Post printing operations

Printed green bodies were osmotically dried in the temperatures range of 50–70 °C in 50 ml of different concentrated PEG solutions, i.e. PEG 200, PEG 400, PEG 600 and PEG 2000, for a certain amount of time and then air dried for 24 h at 30 °C (Fig. 3).

Finally, samples were debinded at 400 °C and sintered at 1550 °C for 4 h in air following the procedure previously reported [13,35].

2.5. Characterizations

Viscosity of printable inks was determined by recording the flow curves at 25 °C in the range of 0.01–100 s^{-1} through a rotational rheometer with controlled shear stress, C-VOR 120 Bohlin (Malvern Instruments, UK), using a parallel plate geometry (1 mm gap) with a top

plate diameter of 20 mm (PP20) and a solvent trap to avoid any water evaporation phenomena during the test. Storage (G') and loss (G'') modulus were determined through stress sweep tests conducted in the 0.1–1000 Pa range using a flat cone geometry (0.150 mm gap) with a top plate diameter of 40 mm with an angle of 4° and the solvent trap.

TG analyses, performed to assess the solid content of the obtained pastes, were carried-out with a Simultaneous Thermal Analyser STA 449 F3 Jupiter (Netzsch, Selb/Bavaria, Germany) at a heating rate of 5 °C/min from ambient temperature to 1100 °C under air flux.

Morphological characterizations of green, debinded and sintered samples were carried out using a three-dimensional digital microscope (RH 2000, HIROX, Japan), equipped with the image analysis software RH-2000 (ver 2.0.3.0) used for the determination of the extruded filaments diameter, mesh sizes and the free space provided by the network of the resulted structures.

Sintered bodies were also analyzed by XRD analysis (D8 ADVANCE, LynkEye Detector-Bruker AXS, Germany) using $\text{CuK}\alpha$ radiation in the 20–80° 2θ range and a scan rate of 0.02°, and by scanning electron microscope SIGMA SEM-FEG (Zeiss). Before XRD analysis, the sintered samples were manually grounded and sieved through 75 μm mesh to obtain the corresponding powders.

Density of sintered samples was measured by Archimedes' method in distilled water at 25 °C.

Nanoindentation tests were carried out to characterize the local mechanical properties, Elastic Modulus (E) and Hardness (H) of the cer-cer composite structures produced using the nanoindenter XP™ (MTS Systems Corporation, Oak Ridge, TN, USA) equipped with a Berkovich diamond tip. Before the tests, samples were polished using progressively finer abrasive diamond suspensions up to 1 μm , and finally treated with a colloidal silica suspension to achieve a mirror-like surface finish. Moreover, the area function of the indenter tip was calibrated on a

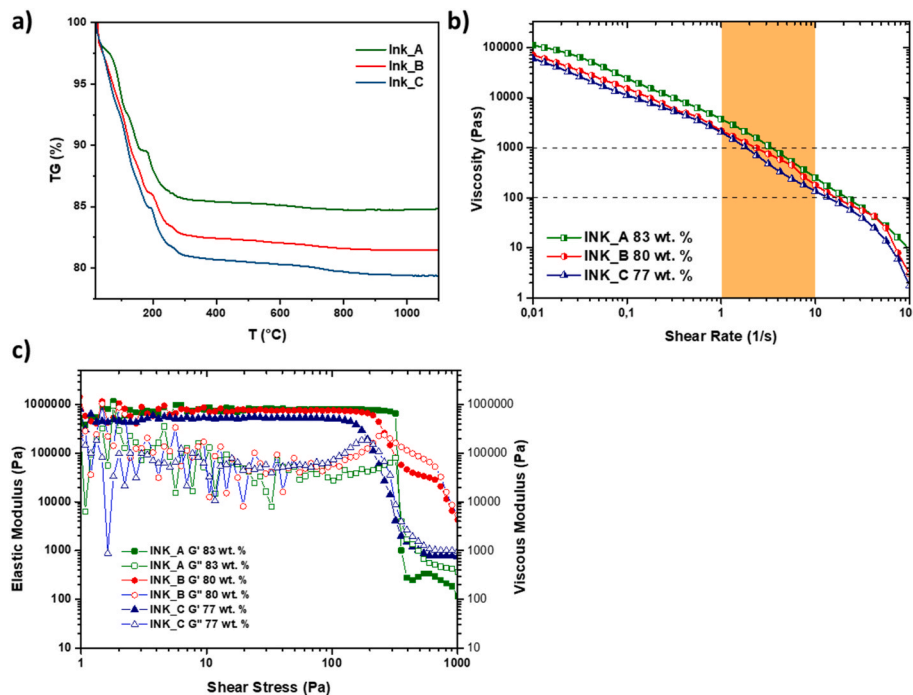


Fig. 4. Thermogravimetric analysis (a); viscosity curves (b) and G' and G'' vs shear stress measured at 1 Hz (c) for the three different inks.

standard fused silica specimen. Results of E and H for each indentation were analyzed with the Oliver and Pharr method [36], considering a Poisson's ratio of 0.33.

Two series of mechanical tests using a nanoindenter XP were carried out to determine the mechanical properties of BCZY-GDC composite at the filament bulk (single-layer structure) and the interface between contiguous filaments (multi-layer structure). For the first series of experiments, 150 indentations, arranged in three 10×5 arrays were performed up to 2000 nm of maximum displacement into the surface. For the second series of experiments, an array of 133 imprints (19×7) at the interface region between two contiguous filaments was performed at the maximum displacement into the surface (2000 nm), to study the influence of the microstructure on the mechanical properties. Measurements were located taking as a reference the distance from the central line of the interface, and a spacing of 50 μm between indentations was chosen to avoid overlapping effects of the plastic flow from neighboring indentations [37,38].

To assess the mechanical contribution of each constituent of the composite (i.e. BCZY, GDC and BCZY-GDC), another series of tests were carried out using the high-speed KLA iMicro nanoindenter (KLA Corp., USA), where each test was conducted in ~ 1 s to obtain maps with 10,000 indentations spaced 1 μm , performed with 3 mN load (corresponding to about 70–120 nm indentation depth). Before the tests, the indenter tip was calibrated and the metallographic samples were polished using the same methodology described above. E and H for each indentation were calculated using Oliver and Pharr's method [36], using a Poisson's ratio of 0.33 for both materials. From the acquired data, mechanical property cartographies were represented for E and H maps as a function of the x -axis and y -axis position.

The data distribution from the large array of high-speed nanoindentation was deconvoluted using the 1D Gaussian fitting to obtain the properties of the individual ceramics and estimate their volume fraction [30,31]. This approach, proposed by Ulm et al. [39–42] assumes that each indentation test may be treated as an independent statistical value, and the indentation depth is much smaller than the most critical phase size [37,38]. First, an experimental cumulative distribution function (CDF) is generated, and mechanical properties (E or H) are approximated by a Gaussian function ($p_i(x)$), identified by the mean

value (μ_i) and standard deviation (σ_i) for each i constitutive phase (Eq. (1)):

$$p_i(x) = \frac{1}{\sqrt{2\pi}\sigma_i} \exp\left(-\frac{(x - \mu_i)^2}{2\sigma_i^2}\right), x = (E, H) \quad (1)$$

Afterwards, x values determined using nanoindentation (i.e. x corresponding to hardness or elastic modulus data) were fitted to CDF using a sigmoid shape error function, as follows (Eq. (2)):

$$CDF = \sum_{i=1}^n \frac{f_i}{2} \operatorname{erf}\left(-\frac{(x - \mu_i)^2}{2\sigma_i^2}\right), x = (E, H) \quad (2)$$

where n is the total number of phases considered and f_i the volume fraction of each i phase (note, the sum of f_i must be equal to one).

In the present work, three different mechanically distinct constituents were considered. Two were related to each component of the composite (i.e. BCZY and GDC) and the third one was attributed to a composite-porosity response associated with indentations located near the porosity, where elastic and plastic flow interact with one or both phases. The estimation of the composite/interface constituent resulted by combining BCZY and GDC was not separated as a fourth constituent, as the mechanical properties of the two phases were too close, with partially overlapping property distributions, resulting in a challenge by using this approach. In addition to the volume fraction of BCZY and GDC, the f_i for the composite-porosity constituent was also numerically estimated by using a simple model, assuming that all the indentations interacting with the porosity present a composite-porosity response.

3. Results and discussion

3.1. Thermal and rheological characterization

Using the optimized mixing methodology described in the “Materials and Methods” section, three homogeneous and stable water-based inks were successfully obtained without using any dispersing agents. Thermogravimetric analyses were performed in order to verify any loss of material during ink preparation (Fig. 4 a). The residual mass at 1100 °C

Table 2

Printing parameters used in this study.

Set-up	Nozzle size (mm)	v (mm/min)	h (mm)	d_{th} (mm)	w (mm)
1	0.41	5	0.80	0.42	0.40
2	0.41	5	0.80	0.42	0.52

**Fig. 5.** Photos of sample micro extruded with a 0.410 mm nozzle with the three ink produced.

is 83.8, 81.5 and 79.4 % for Ink_A, Ink_B and Ink_C respectively, deviating by less than 2% from the theoretical compositions (Table 1) and thus highlighting the suitable reproducibility of the developed production process.

The viscosity of the obtained pastes was evaluated by registering the flow curves (Fig. 4 b). All the systems considered show a pseudoplastic behaviour suitable for inks that must be extruded or injected through reduced diameter nozzles. As expected, the viscosity at low shear stresses increase from $6,7 \cdot 10^4$ Pa s for INK_C to $7,3 \cdot 10^4$ Pa s for INK_B and $11,0 \cdot 10^4$ Pa s for INK_A due to the simultaneous increase in the amount of solid loading (from 77 to 83 wt %) and binder quantity. All the three produced pastes present, in the 1–3 s-1 range, only slightly higher viscosity values compared to the process window reported for the microextrusion of hydrogel-based inks (Fig. 4 b) [43], thus they were considered suitable for the DIW process. G' and G'' as a function of the applied shear stress are reported in Fig. 4 c. At low stress values, all the three inks exhibit a linear viscoelastic response (LVR) with $G' > G'' = 4, 5-8,0 \cdot 10^5$ Pa, indicating good stiffness of the extruded filaments at rest. As the stress amplitude rises (i.e. above 150 Pa), G' starts decreasing. This point corresponds to the yield stress (τ_y) of the Ink and represents the maximum stress that the ink can support without suffering irreversible deformation. Increasing the solid loading, τ_y occurs at 172 Pa, 235 Pa and 320 Pa for INK_C, INK_B and INK_A respectively, indicating the possibility to produce multilayer structures without collapsing with each paste produced. Looking at the end of the LVR, all the inks show a

sharp overshoot of the G'' in the vicinity of the critical stress resulting from the development of a colloidal structure and aggregates of ceramic particles during the stress sweep tests [44]. From a rheological point of view, all the three ink produced where considered acceptable for subsequent printing tests.

3.2. 3D printing of BCZY-GDC structures

As observed by Hong et al. [45], the gaps between extruded filaments (w) can be eliminated by controlling the filament spacing and the distance between the needle tip and the substrate, according to the following equation (Eq. (3)):

$$d_{th} = \frac{Q}{v \cdot h} \quad (3)$$

where d_{th} is the theoretical filament width, Q is the flow rate (ml/min), v and h the printing rate (mm/min) and height respectively. On the other hand, to obtain grids-type geometries with the desired mesh size, it is necessary to set the distance between extruded filaments (w) greater than d_{th} . The Optimized printing parameters, used in this study, are reported in Table 2. Porous honeycomb-type structures (Fig. 2 a-b) where obtained with set-up 1, while grid-type geometries (Fig. 2 d) were obtained with set-up 2.

Fig. 5 shows samples micro extruded through 0.41 mm diameter nozzle with set up 1, while Fig. 6 shows the difference between the two different sets of printing parameters for grid-type geometry. Optical micrographs show quite homogeneous filament diameters of 0.423 ± 0.07 mm, very similar values to those calculated through Eq. (1) indicating a good correlation between the predicted and the experimentally obtained extruded diameter. The “pattern” observed on the lower surface of the samples, results from the contact with the starting substrate which is not perfectly smooth. Several single and multilayer structures where successful printed in different shapes without nozzle clogging, and then subjected to drying and thermal treatments.

3.3. Post printing operations

In most of water-based processes, drying is generally the bottleneck and requires the use of ad-hoc instrumentations to adequately control the release of water from the structures. Non-uniform and differential drying speed in various regions due to the solvent gradient, induces structural and residual stresses which cause distortions and cracks [46].

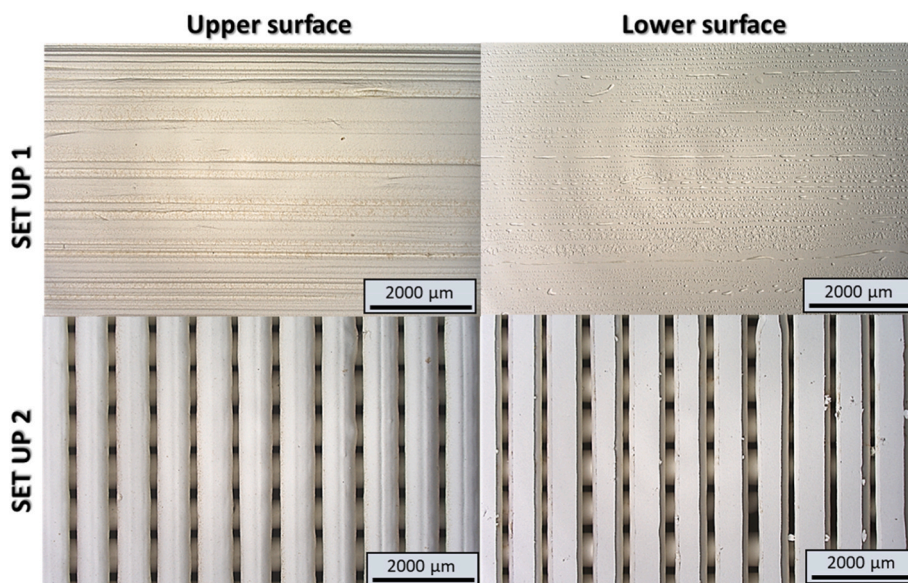
**Fig. 6.** Optical micrographs of the upper and lower surface of a sample micro extruded with Ink_B with the two different printing parameter's set-up.

Table 3

Summary of the osmotic drying tests.

	INK_A (83 wt %)	INK_B (80 wt %)	INK_C (77 wt %)
Liquid desiccants			
PEG 200	✓	✓	X
PEG 400	X	X	X
PEG 600	X	X	X
PEG 2000	X	X	X
T optimal	60 °C	60 °C	55 °C
Drying time	18 h	24 h	72 h

✓: without defects; X: cracks formation.

These defects can be minimised or eliminated by using the liquid desiccant drying method due to the release of residual stresses [47]. In this method, the wet green parts are brought into contact with an appropriate liquid desiccant (typically PEG) by immersion, and water is extracted by an osmotic mechanism due to the different chemical potential of water in the green body and the surrounding solution. After printing, samples were poured in different warm PEG solution for a certain amount of time and then air dried for 24 h at 30 °C. Results are summarized in Table 3 while Fig. 7 shows the optical images of samples after osmotic drying. The data (Table 3) indicate that PEG 200 was the only fluid capable of drying samples printed with Ink_A and Ink_B without cracks or malformations (Fig. 7a and b), and the drying time depends on the amount of water inside the samples. However, in the range of investigated conditions it was not possible to successful dry samples obtained with Ink_C (Fig. 7c). This is probably related to the

higher amount of water present in this paste that requires longer drying time and thus the possible diffusion of some PEG molecules in the hydrogel that must be removed to avoid the formation of defects [33]. Samples were then subjected to debinding at 400 °C and sintering up to 1550 °C for 4 h.

Further investigations are still in progress to optimize the osmotic drying of samples with high water content such as Ink_C; only Ink_A and Ink_B were considered in the subsequent stages of the work.

3.4. Microstructural characterizations

The optical images of the upper and lower parts of the sintered samples are reported in Fig. 8. No macroscopic defects are visible neither on the upper surface in contact with air, nor in the one facing the platinum substrate. Moreover, looking at the fracture and the polished cross-section of a multilayer sample (Fig. 9 a-b), no signs of interlayer delamination are notable indicating an excellent adhesion between each extruded filament. Polished cross-sections (Fig. 9 c-d) reveals also micrometric sized grains of $1,02 \pm 0,47$ and $1,04 \pm 0,45$ μm respectively for samples produced with Ink_A and Ink_B and randomly distributed pin holes for both the compositions, representing the residual porosity. Scaffold densities were than measured by Archimedes' method and found to be $95,0 \pm 1,0$ and $93,2 \pm 2,0$ % for Ink_A and Ink_B respectively. The free-space provided by the network (P_N) [34] was geometrically calculated for each selected designs and reported in Table 4. Values are in good agreement with those fixed in the printing set up, showing high shape retention of water based BCZY-GDC inks. Furthermore, XRD analysis performed on the post-sintering samples show no

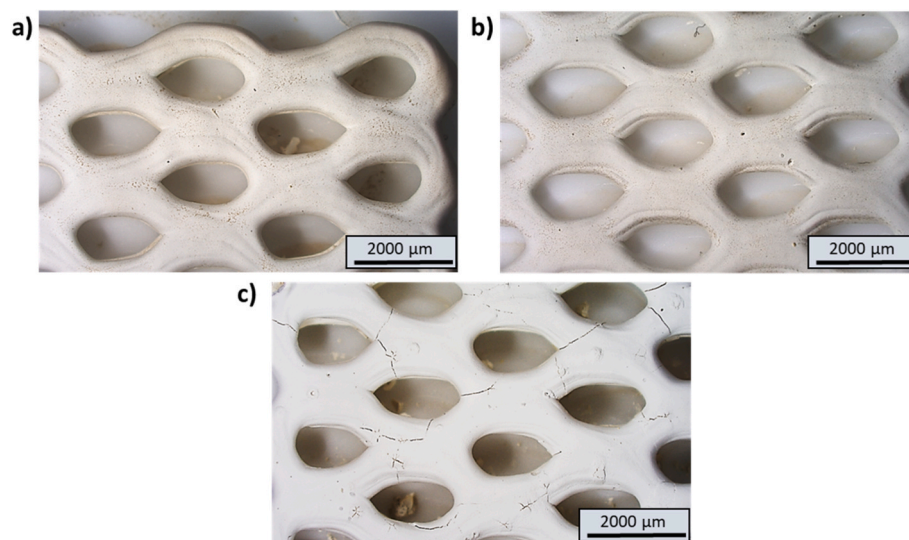


Fig. 7. Optical micrographs of samples micro extruded using set-up 1 with (a) Ink_A, (b) Ink_B and (c) Ink_C in “small” hexagonal geometry after optimized osmotic drying treatment.

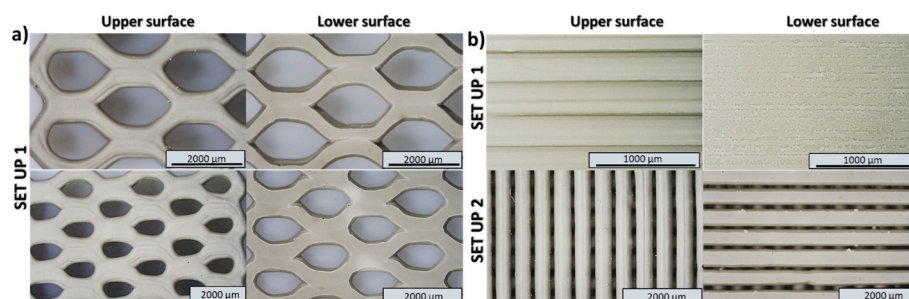


Fig. 8. Optical microscope of the upper and lower surface of samples after sintering printed with (a) Ink_A and (b) Ink_B.

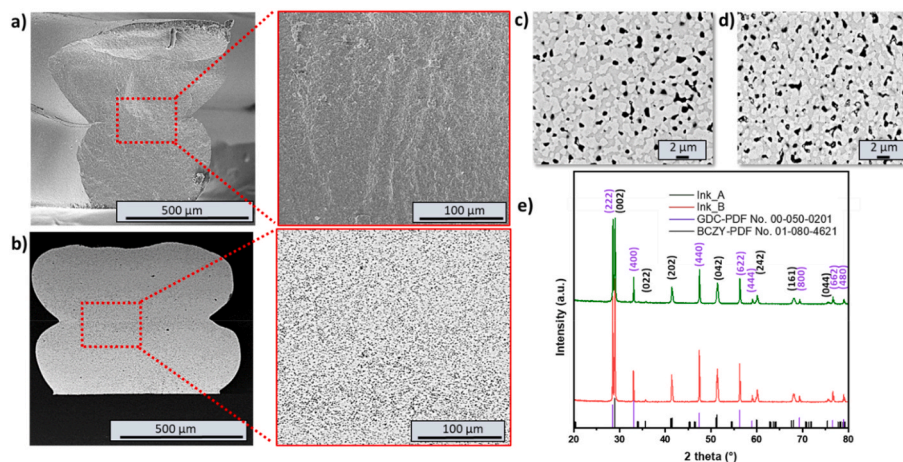


Fig. 9. SEM micrographs of the fracture surface (a) and polished cross section (b) of a two layered sample printed with Ink_A. SEM micrographs (BSE mode) of the polished cross section of sintered Ink_A (c) and Ink_B (d); XRPD pattern of the final 3D printed structures (e).

Table 4

Free network space calculated for sintered samples, compared with the fixed porosity values of the developed designs.

Design	P _N * (%)	Fixed porosity
Large hexagonal mesh (3.5 × 2.0 mm ²)	43 ± 2	45
Small hexagonal mesh (2.6 × 1.5 mm ²)	33 ± 2	30
Fine grids (0.1 × 0.1 mm ²)	17 ± 2	15

secondary phases (Fig. 9 d), indicating that the whole formulation process did not affect the perovskite-fluorite phases purity.

3.5. Nanoindentation tests

The mechanical properties of BCZY-GDC were assessed at micro-/nanometric scale using the nanoindentation technique. Fig. 10 shows the evolution of the E and the H as a function of the indentation depth for a single-layer structure of BCZY-GDC. While the elastic modulus of the composite presented an almost constant tendency with the indentation depth, hardness values exhibited a significant drop with the increase of indentation depth. The trend registered for H values was attributed to the effect of the porosity in the microstructure, which was in good agreement with relative densities close to 93–95%. A high dispersion in both mechanical properties was obtained at low indentation depth, due to the presence of two constituent ceramics with different mechanical properties. In contrast, the mechanical response measured at large indentation depths was related to a combined behaviour of the two ceramics and the porosity, thus resulting in a low dispersion in both E and H .

The mechanical response at the interface region between two

contiguous filaments were also studied, as the contact point between extruded parts could be a weak point in the processing of ceramics through DIW. Fig. 11a shows the indented area of a multilayer sample, while Fig. 11b and c shows the elastic modulus and hardness profiles registered into the cross-section, respectively. A similar tendency in the distribution of E and H was observed, and values exhibit a significant symmetry to the central line of the interface. Compared with the mechanical properties of the filament bulk in a single-layer structure, only a small decrease in both E and H (<5%) was found in the contact point between filaments which confirms the good optimization of the processing parameters.

3.6. Mechanical property maps and 1D Gaussian fitting

Fig. 12 shows the E and H maps obtained through iMicro nano-indenter at 3 mN controlled load. Both maps present values within a relatively wide range, as a result of two ceramic constituents with different mechanical properties and the presence of porosity. Moreover, a homogeneous spatial distribution in the mechanical properties of the composite were also observed. This is in good agreement with the observed cross section (Fig. 9), suggesting a good optimization of the material processing which leads to the obtainment of a homogeneous distribution of both the two phases in the whole composite. It is also important to note that a homogeneous spatial distribution of both BCZY and GDC phases together with a uniform distribution of the mechanical properties is of paramount importance for an ion-electron conductive ceramic membrane, to guarantee remarkable electrochemical performance and good mechanical reliability during in-service operations.

The intrinsic properties of the individual constituents of the BCZY-GDC composite from the indentation data were determined by

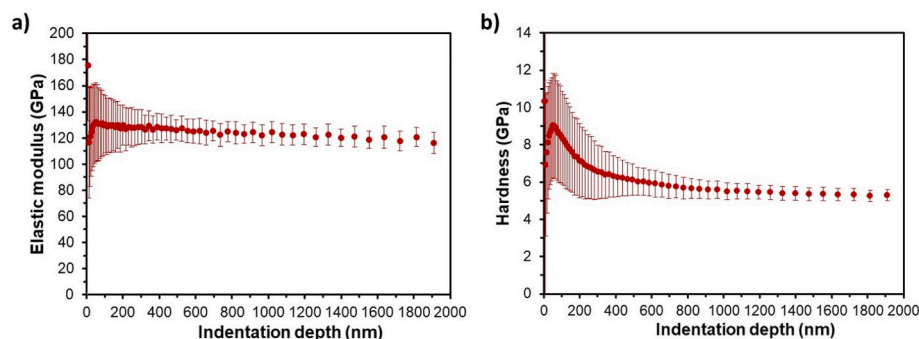


Fig. 10. (a) Elastic Modulus and (b) Hardness as a function of the indentation depth for the BCZY-GDC composite in a single-layer structure sample.

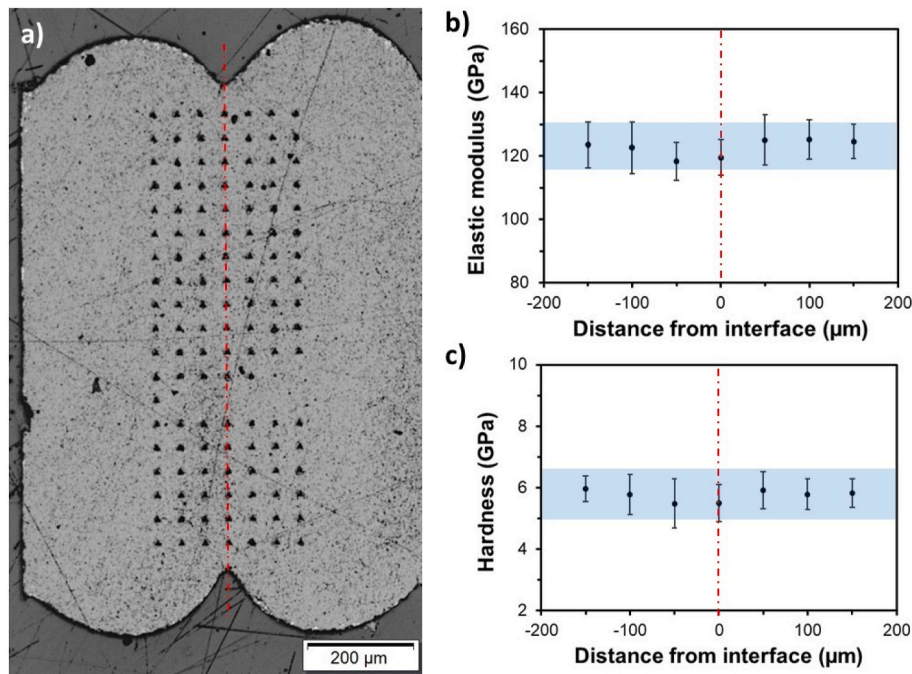


Fig. 11. (a) Optical micrograph of a multilayer polished cross section, mechanically tested in an array of 19x7: the interface between the two printed filaments is highlighted by a red dash-dot line. (b) Elastic Modulus and (c) hardness as a function of the distance from the interface between filaments. The red dash-dot line indicates the interface between printed filaments, and the blue region marks the average mechanical property with the corresponding standard deviation. (For interpretation of the references to colour in this figure legend, the reader is referred to the Web version of this article.)

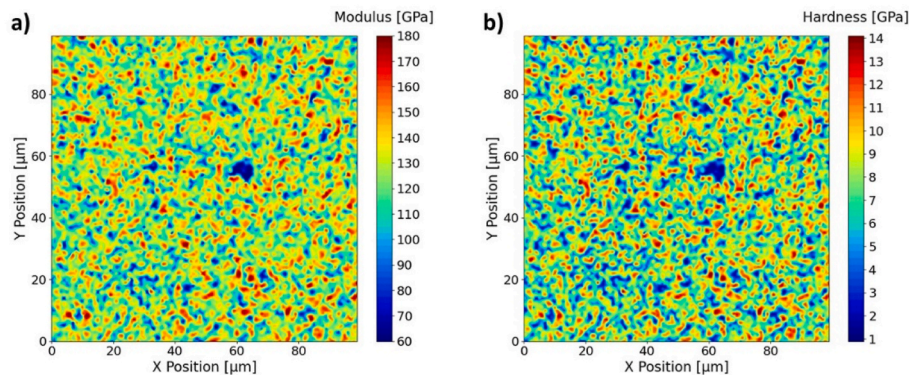


Fig. 12. (a) Elastic modulus and (b) hardness maps determined by iMicro nanoindenter at 3 mN of maximum applied load.

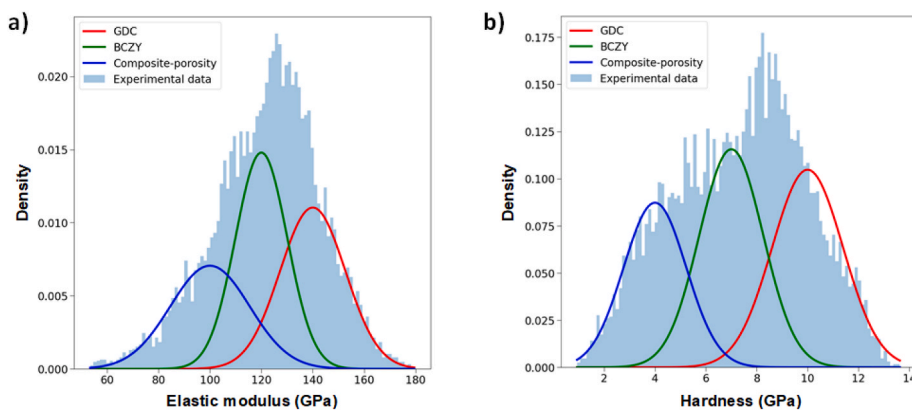


Fig. 13. (a) Elastic modulus and (b) hardness for BCZY-GDC with a constant bin size of 1 GPa for elastic modulus and 0.1 GPa for hardness determined from 10,000 indents performed at 3 mN of maximum applied load.

Table 5

Elastic modulus, Hardness and volume fraction calculated using the 1D Gaussian method.

Constituent	<i>E</i> (GPa)	<i>f_i</i>	<i>H</i> (GPa)	<i>f_i</i>
BCZY	122 ± 10	0.374	7.2 ± 1.3	0.364
GDC	141 ± 13	0.352	9.8 ± 1.4	0.366
Composite-porosity	99 ± 15	0.274	4.1 ± 1.2	0.270

deconvoluting and statistically treating the experimental data. Elastic modulus and hardness histograms of raw data are shown in Fig. 13, together with the 1D Gaussian distributions. The statistical analysis allows the identification of three different constituents in both *E* and *H* properties, such as GDC (harder – red curve), BCZY (intermediate – green curve) and composite-porosity constituents (softer – blue curve). The intrinsic *E* and *H* values obtained by using the 1D Gaussian fitting statistical method are summarized in Table 5. The results were found to be in good agreement with those obtained in the literature for similar ceramic compositions using the nanoindentation technique [8,34,48–51]. Moreover, the volume fraction estimated from the curves was found to be about 0.36 ± 0.10 for both BCZY and GDC, resulting in a BCZY/GDC ratio of 1.0, in accordance with the theoretical volume fraction composition of the original ink. Additionally, the significant volume-fraction value of the composite-porosity constituent gives an idea of the porosity contribution to the mechanical response of the composite.

4. Conclusions

In this work, eco-friendly water-based BCZY-GDC cer-cer composite pastes were successfully obtained and 3D printed for the first time. The optimized mixing methodology, previously developed in our labs for BCZY-UV curable pastes, is reliable, reproducible and, one more time, permitted the production of homogenous microextrusion pastes without dispersing agents or solvents. Moreover, the prediction of the theoretical diameter of the extruded filaments allowed us to obtain two sets of printing parameters suitable to print all the formulated inks in different geometries. Osmotic drying in concentrated PEG solutions has been investigated in order to rapidly obtain defect-free green bodies. Using temperature close to 60 °C and employing PEG 200 it was possible to successfully dry samples produced with Ink_A (83 wt % solid) and Ink_B (80 wt % solid) in less than 24 h without defects formation. Once drying was optimized, planar and crack-free sintered samples were achieved in single or multilayer structures which were mechanically characterized using several nanoindentation techniques. In this regard, intrinsic mechanical properties of BCZY and GDC were determined from the deconvolutions of *E* and *H* data using 1D Gaussian fitting statistical method for the first time. Both *E* and *H* values were found to be close to those obtained in previous works for BaCe_{0.65}Zr_{0.20}Y_{0.15}O_{3-δ}/Gd_{0.15}Ce_{0.85}O_{2-δ} – type ceramics fabricated through traditional shaping techniques. Moreover, the statistical treatment of the data led to the evaluation of the significant volume-fraction value of the composite-porosity constituent, giving an idea of the porosity contribution to the mechanical response of the composite. In addition, the interface between contiguous filaments in the multilayer structure showed similar mechanical behaviour to the filament bulk, confirming the possibility to exploit this process for the fabrication of engineered multilayers supports for hydrogen separation membranes. Further work is ongoing to assess the scalability of the developed process, gas permeation properties of the microextruded samples as well as large scale mechanical properties of 3D-microextruded membranes.

Acknowledgement

This work has been funded by the agreement between the Italian Ministry of Economic Development and the Italian National Research

Council “Ricerca di sistema elettrico nazionale” and the Grants PID2021-126614OB-I00, funded by MCIN/AEI/10.13039/501100011033 and FEDER. Additional funding has been received from AGAUR, Agency for Administration of University and Research (2021 SGR 01053). Miguel Morales is a Serra Hünter Lecturer Professor, and he is grateful to the Serra Hünter program (Generalitat de Catalunya).

References

- [1] F.S. AlHumaidan, M. Absi Halabi, M.S. Rana, M. Vinoba, Blue hydrogen: current status and future technologies, *Energy Convers. Manag.* 283 (2023), 116840, <https://doi.org/10.1016/j.enconman.2023.116840>.
- [2] S. Van Renssen, The hydrogen solution? *Nat. Clim. Change* 10 (2020) 799–801, <https://doi.org/10.1038/s41558-020-0891-0>.
- [3] E. Monteiro, P.S.D. Brito, Hydrogen supply chain: current status and prospects, *Energy Storage* (2023) e466, <https://doi.org/10.1002/est2.466>.
- [4] I. Stenina, A. Yaroslavtsev, Modern technologies of hydrogen production, *Processes* 11 (2022) 56, <https://doi.org/10.3390/pr11010056>.
- [5] Roadmap for Sustainable Mixed Ionic-Electronic Conducting Membranes - Chen - 2022 - Advanced Functional Materials - Wiley Online Library, (n.d.). <https://onlinelibrary.wiley.com/doi/full/10.1002/adfm.202105702> (accessed June 13, 2023).
- [6] Global hydrogen development - a technological and geopolitical overview, *Int. J. Hydrogen Energy* 47 (2022) 7016–7048, <https://doi.org/10.1016/j.ijhydene.2021.12.076>.
- [7] W. Deibert, M.E. Ivanova, S. Baumann, O. Guillon, W.A. Meulenber, Ion-conducting ceramic membrane reactors for high-temperature applications, *J. Membr. Sci.* 543 (2017) 79–97, <https://doi.org/10.1016/j.memsci.2017.08.016>.
- [8] E. Mercadelli, A. Gondolini, M. Ardit, G. Cruciani, C. Melandri, S. Escolástico, J. M. Serra, A. Sanson, Chemical and mechanical stability of BCZY-GDC membranes for hydrogen separation, *Separ. Purif. Technol.* 289 (2022), 120795, <https://doi.org/10.1016/j.seppur.2022.120795>.
- [9] C. Mortalò, E. Rebollo, S. Escolástico, S. Deambrosio, K. Haas-Santo, M. Rancan, R. Dittmeyer, L. Armelao, M. Fabrizio, Enhanced sulfur tolerance of BaCe_{0.65}Zr_{0.20}Y_{0.15}O_{3-δ}-Ce_{0.85}Gd_{0.15}O_{2-δ} composite for hydrogen separation membranes, *J. Membr. Sci.* 564 (2018) 123–132, <https://doi.org/10.1016/j.memsci.2018.07.015>.
- [10] E. Rebollo, C. Mortalò, S. Escolástico, S. Boldrini, S. Barison, J.M. Serra, M. Fabrizio, Exceptional hydrogen permeation of all-ceramic composite robust membranes based on BaCe_{0.65}Zr_{0.20}Y_{0.15}O_{3-δ} and Y- or Gd-doped ceria, *Energy Environ. Sci.* 8 (2015) 3675–3686, <https://doi.org/10.1039/C5EE01793A>.
- [11] C. Mortalò, M. Boaro, E. Rebollo, V. Zin, E. Aneggi, M. Fabrizio, A. Trovarelli, Insights on the interfacial processes involved in the mechanical and redox stability of the BaCe_{0.65}Zr_{0.20}Y_{0.15}O_{3-δ}-Ce_{0.85}Gd_{0.15}O_{2-δ} composite, *ACS Appl. Energy Mater.* 3 (2020) 9877–9888, <https://doi.org/10.1021/acsaem.0c01589>.
- [12] C. Mortalò, A. Santoru, C. Pistidda, E. Rebollo, M. Boaro, C. Leonelli, M. Fabrizio, Structural evolution of BaCe_{0.65}Zr_{0.20}Y_{0.15}O_{3-δ}-Ce_{0.85}Gd_{0.15}O_{2-δ} composite MPEC membrane by in-situ synchrotron XRD analyses, *Mater. Today Energy* 13 (2019) 331–341, <https://doi.org/10.1016/j.mtener.2019.06.004>.
- [13] D. Montaleone, E. Mercadelli, S. Escolástico, A. Gondolini, J.M. Serra, A. Sanson, All-ceramic asymmetric membranes with superior hydrogen permeation, *J. Mater. Chem. A* 6 (2018) 15718–15727, <https://doi.org/10.1039/C8TA04764B>.
- [14] S. Hamakawa, L. Li, A. Li, E. Iglesia, Synthesis and hydrogen permeation properties of membranes based on dense SrCe_{0.95}Yb_{0.05}O_{3-α} thin films, *Solid State Ionics* 148 (2002) 71–81, [https://doi.org/10.1016/S0167-2738\(02\)00047-4](https://doi.org/10.1016/S0167-2738(02)00047-4).
- [15] V. Gil, J. Gurauskis, M.-A. Einarsrud, Asymmetric supported dense lanthanum tungstate membranes, *J. Eur. Ceram. Soc.* 34 (2014) 3783–3790, <https://doi.org/10.1016/j.jeurceramsoc.2014.06.019>.
- [16] C. Gaudillere, J.M. Serra, Freeze-casting: fabrication of highly porous and hierarchical ceramic supports for energy applications, *Bol. Soc. Española Ceram. Vidr.* 55 (2016) 45–54, <https://doi.org/10.1016/j.bsecv.2016.02.002>.
- [17] A. Gondolini, E. Mercadelli, S. Casadio, A. Sanson, Freeze cast support for hydrogen separation membrane, *J. Eur. Ceram. Soc.* 42 (2022) 1053–1060, <https://doi.org/10.1016/j.jeurceramsoc.2021.10.063>.
- [18] F. Schulze-Küppers, U.V. Unije, H. Blank, M. Balaguer, S. Baumann, R. Mücke, W. A. Meulenber, Comparison of freeze-dried and tape-cast support microstructure on high-flux oxygen transport membrane performance, *J. Membr. Sci.* 564 (2018) 218–226, <https://doi.org/10.1016/j.memsci.2018.07.028>.
- [19] A. Gondolini, A. Bartoletti, E. Mercadelli, P. Gramazio, A. Fasolini, F. Basile, A. Sanson, Development and hydrogen permeation of freeze-cast ceramic membrane, *J. Membr. Sci.* 684 (2023), 121865, <https://doi.org/10.1016/j.memsci.2023.121865>.
- [20] Y. Lakhdar, C. Tuck, J. Binner, A. Terry, R. Goodridge, Additive manufacturing of advanced ceramic materials, *Prog. Mater. Sci.* 116 (2021), 100736, <https://doi.org/10.1016/j.pmatsci.2020.100736>.
- [21] M. Mariani, R. Beltrami, E. Migliori, L. Cangini, E. Mercadelli, C. Baldisserri, C. Galassi, N. Lecis, Additive manufacturing of lead-free KNN by binder jetting, *J. Eur. Ceram. Soc.* 42 (2022) 5598–5605, <https://doi.org/10.1016/j.jeurceramsoc.2022.05.075>.
- [22] A. Ambrosi, M. Pumera, 3D-printing technologies for electrochemical applications, *Chem. Soc. Rev.* 45 (2016) 2740–2755, <https://doi.org/10.1039/C5CS00714C>.
- [23] E. Peng, D. Zhang, J. Ding, Ceramic robocasting: recent achievements, potential, and future developments, *Adv. Mater.* 30 (2018), 1802404, <https://doi.org/10.1002/adma.201802404>.

- [24] M. Cannio, C. Mortalò, M. Prestianni, F. Andreola, S.M. Deambrosis, E. Miorin, V. Zin, D.N. Boccaccini, M. Romagnoli, Manufacturing of BaCe_{0.65}Zr_{0.20}Y_{0.15}O_{3-δ}-Ce_{0.85}Gd_{0.15}O_{2-δ} structures by micro-extrusion 3D-printing, *Mater. Lett.* 284 (2021), 128970, <https://doi.org/10.1016/j.matlet.2020.128970>.
- [25] J.J. Roa, P. Sudharshan Phani, W.C. Oliver, L. Llanes, Mapping of mechanical properties at microstructural length scale in WC-Co cemented carbides: assessment of hardness and elastic modulus by means of high speed massive nanoindentation and statistical analysis, *Int. J. Refract. Metals Hard Mater.* 75 (2018) 211–217, <https://doi.org/10.1016/j.jrmhm.2018.04.019>.
- [26] B. Vignesh, W.C. Oliver, G.S. Kumar, P.S. Phani, Critical assessment of high speed nanoindentation mapping technique and data deconvolution on thermal barrier coatings, *Mater. Des.* 181 (2019), 108084, <https://doi.org/10.1016/j.matdes.2019.108084>.
- [27] J. Němeček, J. Lukeš, J. Němeček, High-speed mechanical mapping of blended cement pastes and its comparison with standard modes of nanoindentation, *Mater. Today Commun.* 23 (2020), 100806, <https://doi.org/10.1016/j.mtcomm.2019.100806>.
- [28] H. Besharatloo, M. Carpio, J.-M. Cabrera, A.M. Mateo, G. Fargas, J.M. Wheeler, J. J. Roa, L. Llanes, Novel mechanical characterization of austenite and ferrite phases within duplex stainless steel, *Metals* 10 (2020) 1352, <https://doi.org/10.3390/met10101352>.
- [29] H. Besharatloo, J.M. Wheeler, Influence of indentation size and spacing on statistical phase analysis via high-speed nanoindentation mapping of metal alloys, *J. Mater. Res.* 36 (2021) 2198–2212, <https://doi.org/10.1557/s43578-021-00214-5>.
- [30] S. Gordon, H. Besharatloo, J.M. Wheeler, T. Rodriguez-Suarez, J.J. Roa, E. Jiménez-Piqué, L. Llanes, Micromechanical mapping of polycrystalline cubic boron nitride composites by means of high-speed nanoindentation: assessment of microstructural assemblage effects, *J. Eur. Ceram. Soc.* 43 (2023) 2968–2975, <https://doi.org/10.1016/j.jeurceramsoc.2022.08.047>.
- [31] L. Silvestroni, N. Gilli, A. Sangiorgi, A. Corozzi, S. Filipović, N. Obradović, L. Ortiz-Membrado, E. Jiménez-Piqué, W.G. Fahrenholtz, Multi-phase (Zr,Ti,Cr)B₂ solid solutions: preparation, multi-scale microstructure, and local properties, *Journal of Advanced Ceramics* 12 (2023) 414–431, <https://doi.org/10.26599/JAC.2023.9220695>.
- [32] C. Tromas, M. Arnoux, X. Milhet, Hardness cartography to increase the nanoindentation resolution in heterogeneous materials: application to a Ni-based single-crystal superalloy, *Scripta Mater.* 66 (2012) 77–80, <https://doi.org/10.1016/j.scriptamat.2011.09.042>.
- [33] H. Xie, X. Yang, P. Liu, X. Xu, Z. Zhou, W. Zhao, Z. Shen, 3D gel printing of alumina ceramics followed by efficient multi-step liquid desiccant drying, *J. Eur. Ceram. Soc.* 41 (2021) 6634–6640, <https://doi.org/10.1016/j.jeurceramsoc.2021.05.034>.
- [34] A. Bartoletti, A. Sangiorgi, A. Gondolini, E. Mercadelli, S. Casadio, S. García-González, M. Morales, E. Jimenez-Pique, A. Sanson, Dispersant- and solvent-free pastes for UV-assisted micro-extrusion of porous proton conductive membrane supports, *J. Eur. Ceram. Soc.* 43 (2023) 4844–4853, <https://doi.org/10.1016/j.jeurceramsoc.2023.04.038>.
- [35] D. Montaleone, E. Mercadelli, A. Gondolini, M. Ardit, P. Pinasco, A. Sanson, Role of the sintering atmosphere in the densification and phase composition of asymmetric BCZY-GDC composite membrane, *J. Eur. Ceram. Soc.* 39 (2019) 21–29, <https://doi.org/10.1016/j.jeurceramsoc.2018.01.043>.
- [36] W.C. Oliver, G.M. Pharr, An improved technique for determining hardness and elastic modulus using load and displacement sensing indentation experiments, *J. Mater. Res.* 7 (1992) 1564–1583, <https://doi.org/10.1557/JMR.1992.1564>.
- [37] J.H. Westbrook, H. Conrad, *The Science of Hardness Testing and its Research Applications*, American Society for Metals, 1973.
- [38] P. Sudharshan Phani, W.C. Oliver, A critical assessment of the effect of indentation spacing on the measurement of hardness and modulus using instrumented indentation testing, *Mater. Des.* 164 (2019), 107563, <https://doi.org/10.1016/j.matdes.2018.107563>.
- [39] G. Constantinides, F.-J. Ulm, K. Van Vliet, On the use of nanoindentation for cementitious materials, *Mater. Struct.* 36 (2003) 191–196, <https://doi.org/10.1007/BF02479557>.
- [40] G. Constantinides, K.S. Ravi Chandran, F.-J. Ulm, K.J. Van Vliet, Grid indentation analysis of composite microstructure and mechanics: principles and validation, *Mater. Sci. Eng., A* 430 (2006) 189–202, <https://doi.org/10.1016/j.msea.2006.05.125>.
- [41] G. Constantinides, F.-J. Ulm, The nanogranular nature of C–S–H, *J. Mech. Phys. Solid.* 55 (2007) 64–90, <https://doi.org/10.1016/j.jmps.2006.06.003>.
- [42] F.-J. Ulm, M. Vandamme, C. Bobko, J. Alberto Ortega, K. Tai, C. Ortiz, Statistical indentation techniques for hydrated nanocomposites: concrete, bone, and shale, *J. Am. Ceram. Soc.* 90 (2007) 2677–2692, <https://doi.org/10.1111/j.1551-2916.2007.02012.x>.
- [43] L. del-Mazo-Barbara, M.-P. Ginebra, Rheological characterisation of ceramic inks for 3D direct ink writing: a review, *J. Eur. Ceram. Soc.* 41 (2021) 18–33, <https://doi.org/10.1016/j.jeurceramsoc.2021.08.031>.
- [44] Y. Eom, F. Kim, S.E. Yang, J.S. Son, H.G. Chae, Rheological design of 3D printable all-inorganic inks using BiSbTe-based thermoelectric materials, *J. Rheol.* 63 (2019) 291–304, <https://doi.org/10.1122/1.5058078>.
- [45] Y. Hong, J. Lei, M. Heim, Y. Song, L. Yuan, S. Mu, R.K. Bordia, H. Xiao, J. Tong, F. Peng, Fabricating ceramics with embedded microchannels using an integrated additive manufacturing and laser machining method, *J. Am. Ceram. Soc.* 102 (2019) 1071–1082, <https://doi.org/10.1111/jace.15982>.
- [46] A. Barati, M. Kokabi, M.H.N. Famili, Drying of gelcast ceramic parts via the liquid desiccant method, *J. Eur. Ceram. Soc.* 23 (2003) 2265–2272, [https://doi.org/10.1016/S0955-2219\(03\)00045-1](https://doi.org/10.1016/S0955-2219(03)00045-1).
- [47] M. Trunec, Osmotic drying of gelcast bodies in liquid desiccant, *J. Eur. Ceram. Soc.* 31 (2011) 2519–2524, <https://doi.org/10.1016/j.jeurceramsoc.2011.02.015>.
- [48] M. Morales, J. Roa, X. Capdevila, M. Segarra, S. Piñol, Effect of sintering temperature on the mechanical properties of film Gd_{0.2}Ce_{0.8}O_{1.9} electrolyte for SOFCs using nanoindentation, *J. N. Mater. Electrochem. Syst.* 12 (2009) 187–193.
- [49] M. Morales, J.J. Roa, X.G. Capdevila, M. Segarra, S. Piñol, Mechanical properties at the nanometer scale of GDC and YSZ used as electrolytes for solid oxide fuel cells, *Acta Mater.* 58 (2010) 2504–2509, <https://doi.org/10.1016/j.actamat.2009.12.036>.
- [50] P.-F. Yang, D.-L. Chen, S.-R. Jian, S.-W. Lee, C.-J. Tseng, Mechanical properties of Ba_{1-x}K_xCe_{0.6}Zr_{0.2}Y_{0.2}O_{3-δ} oxides by nanoindentation, *Procedia Eng.* 79 (2014) 599–605, <https://doi.org/10.1016/j.proeng.2014.06.385>.
- [51] W. Zhou, J. Malzbender, F. Zeng, W. Deibert, O. Guillon, R. Schwaiger, W. A. Meulenbergh, Mechanical properties of BaCe_{0.65}Zr_{0.2}Y_{0.15}O_{3-δ} proton-conducting material determined using different nanoindentation methods, *J. Eur. Ceram. Soc.* 40 (2020) 5653–5661, <https://doi.org/10.1016/j.jeurceramsoc.2020.07.044>.